

# Rational Design of Cathode Structure for High Rate Performance Lithium–Sulfur Batteries

Hongwei Chen,<sup>†,‡</sup> Changhong Wang,<sup>†,‡</sup> Yafei Dai,<sup>‡</sup> Shengqiang Qiu,<sup>§</sup> Jinlong Yang,<sup>||</sup> Wei Lu,<sup>†</sup> and Liwei Chen<sup>\*,†</sup>

<sup>†</sup>*i*-Lab, Suzhou Institute of Nano-Tech and Nano-Bionics (SINANO), Chinese Academy of Sciences, Suzhou 215123, China

<sup>‡</sup>Jiangsu Key Laboratory of Optoelectronic Technology, School of Physics Science & Technology, Nanjing Normal University, Nanjing 210023, China

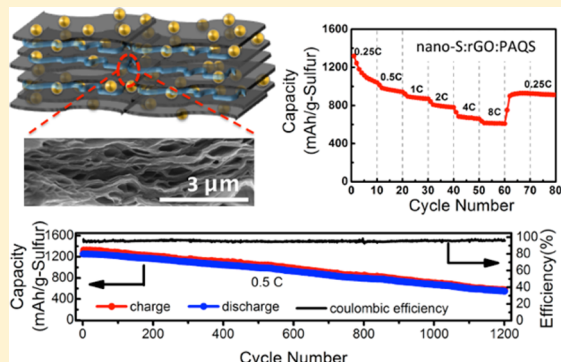
<sup>§</sup>Key Laboratory of Nanodevices and Applications, Suzhou Institute of Nano-Tech and Nano-Bionics (SINANO), Chinese Academy of Sciences, Suzhou 215123, China

<sup>||</sup>Hefei National Laboratory for Physical Sciences at Microscale, University of Science and Technology of China, Hefei, Anhui 230026, China

## S Supporting Information

**ABSTRACT:** Practical applications of Li–S batteries require not only high specific capacities and long cycle lifetimes but also high rate performance. We report a rationally designed Li–S cathode, which consists of a freestanding composite thin film assembled from S nanoparticles, reduced graphene oxide (rGO), and a multifunctional additive poly(antraquinonyl sulfide) (PAQS). The S nanoparticles provide a high initial specific capacity, and the layered and porous rGO structure provides electron and ion transport paths and restricts polysulfide shuttling. PAQS is not only a highly efficient sulfide trapping agent but also an excellent Li<sup>+</sup> conductor, which benefits the battery reaction kinetics at a high rate. The resulting cathode exhibits an initial specific capacity of 1255 mAh g<sup>-1</sup> with a decay rate as low as 0.046% per cycles over 1200 cycles. Importantly, it displays a reversible capacity of 615 mAh g<sup>-1</sup> when discharged at a high rate of 8 C (13.744 A g<sup>-1</sup>).

**KEYWORDS:** Li–S battery, rate performance, free-standing cathode, reduced graphene oxide (rGO), poly(antraquinonyl sulfide) (PAQS), sulfur trapping agent



As one of the most intensely investigated technologies in the electrochemical energy storage field, lithium–sulfur (Li–S) batteries have observed rapid improvements in their properties in recent years.<sup>1–4</sup> Recent work experimentally realized the theoretical specific capacity of 1672 mAh g<sup>-1</sup> using elemental octaatomic S<sub>8</sub> as the cathode material.<sup>5</sup> Highly stable Li–S cathodes with lifetimes of more than 1000 cycles were also reported.<sup>6</sup> Li–S pouch batteries have achieved high energy densities in the range of 350–450 Wh kg<sup>-1</sup>.<sup>7</sup> Although the cycling stability of Li anodes is still an important issue to address,<sup>3,7,8</sup> state-of-the-art performance should, in principle, enable niche applications that do not require particularly long cycling. However, such applications have not been possible with the exception of very selected cases because of the slow discharge rate inhibits the practical application of Li–S technology due to the limitations of the cathode.

In principle, the rate performance of Li–S batteries is significantly affected by polysulfide redox kinetics at the cathode as well as electron and ion transport in the electrodes and electrolyte.<sup>3,10,11</sup> Previous works have shown that, due to the inherent insulating nature of elemental sulfur and the reduction product Li<sub>2</sub>S as well as poor electrode kinetics, there exists a trade-off between rate performance and energy density.<sup>5,12</sup> To improve both properties simultaneously, sufficient redox sites inside the cathode are necessary to promote high energy density, and integrated electron/ion pathways are essential to enhance electrode kinetics.<sup>13–19</sup> Here, we report the rational design and implementation of a Li–S cathode structure that exhibits significantly improved rate

**Received:** May 10, 2015

**Revised:** June 29, 2015

**Published:** July 6, 2015

performance while maintaining a high specific capacity and long cycle lifetime.

As illustrated in Figure 1, the cathode structure consists of a freestanding composite film assembled from S nanoparticles,

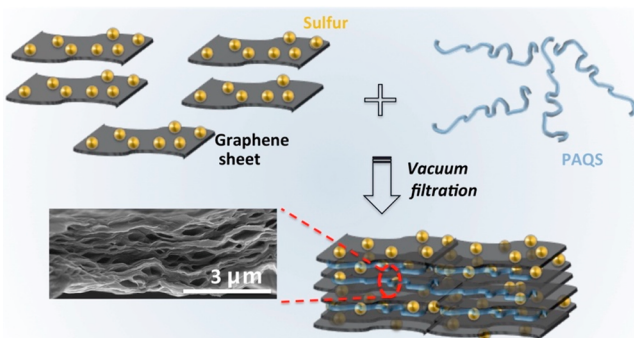


**Figure 1.** Schematic illustration of the nano-S:rGO:PAQS composite thin film cathode. A PAQS polymer solution is mixed with nano-S on an rGO dispersion and vacuum filtered to assemble a freestanding film with a layered and porous structure.

reduced graphene oxide (rGO) and a multifunctional additive poly(anthraquinonyl sulfide) (PAQS). Freestanding cathode structures based on carbon nanomaterials, which can be directly assembled into coin cells without using a metal current collector or carbon paste as a conducting agent, have been previously reported.<sup>20–22</sup> The nanosized S particles improve the degree of S utilization and the initial specific capacity. The layered and porous rGO structure not only restricts polysulfide diffusion but also provides space to accommodate volume changes of the active material during cycling, both of which are beneficial for cycling stability.<sup>14,23</sup> The addition of PAQS is critical to the design of this cathode structure demonstrated here. The PAQS additive may also restrict polysulfide diffusion and prolong the cycling lifetime. Furthermore, PAQS is also a good Li<sup>+</sup> conductor, which facilitates ion transport at high discharging rates.<sup>24,25</sup> The layered rGO structure ensures the electronic conductivity of the electrode, while the interconnected pores provide reservoirs for the electrolyte and constitute connected open pathways for ion transport.<sup>26–30</sup> The nanosized sulfur particles are proven to promote high rate performance. Thus, the holistic design approach will provide a solution for Li–S cathodes with high energy densities, long cycle lifetimes, and excellent rate performances for use in practical applications.

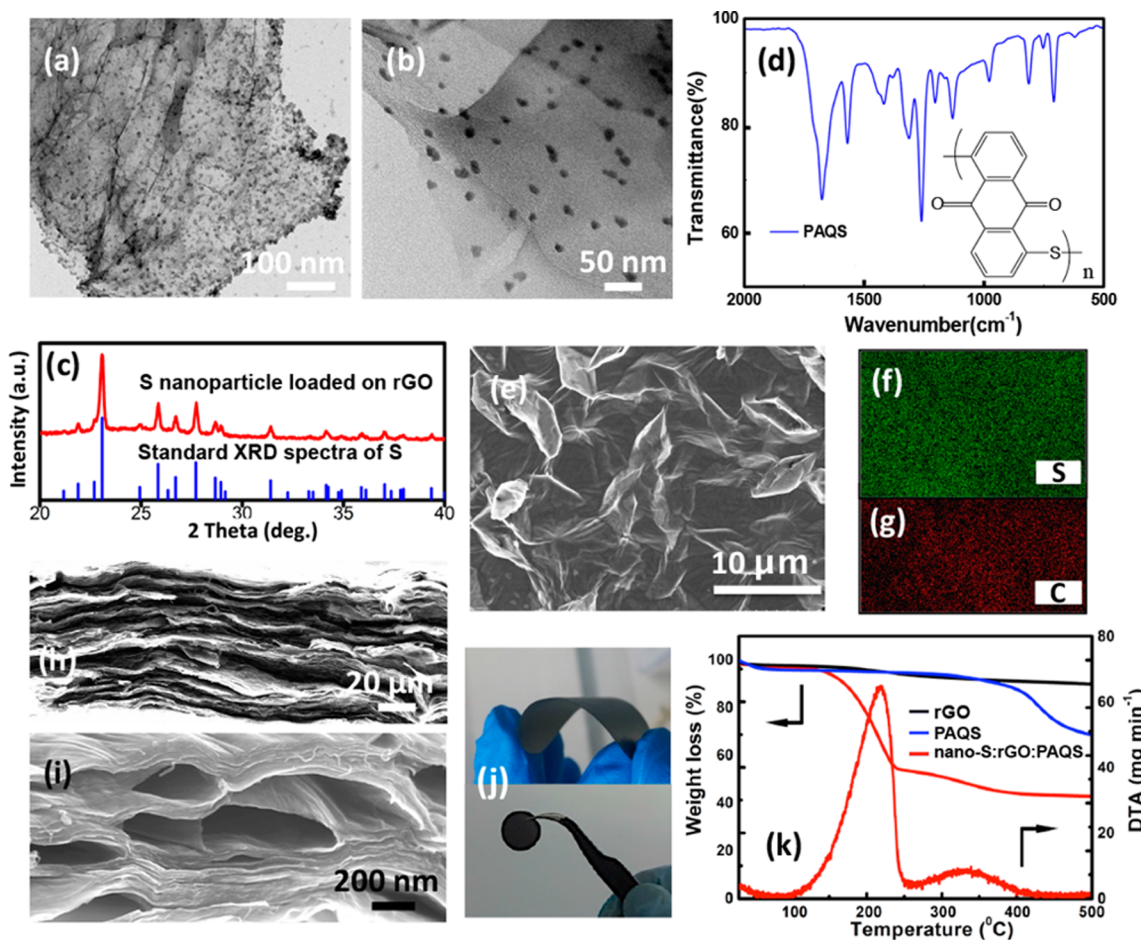


**Figure 2.** Characterization of the nano-S:rGO:PAQS composite thin film cathode. (a), (b) TEM images of S nanoparticles loaded on rGO. (c) XRD pattern of S nanoparticles loaded on rGO. (d) FTIR spectrum of PAQS. (e) SEM image of the top view of the nano-S:rGO:PAQS film. (f, g) EDX mapping of S and C in the nano-S:rGO:PAQS film in the region shown in (e). (h), (i) SEM cross-section view of a nano-S:rGO:PAQS film. (j) Photographs of a nano-S:rGO:PAQS film. Top: the obtained freestanding film. Bottom: the film was punched into smaller cathode disk with diameter of 1.5 cm. (k) TG analyses of nano-S:rGO:PAQS compared with rGO and PAQS.

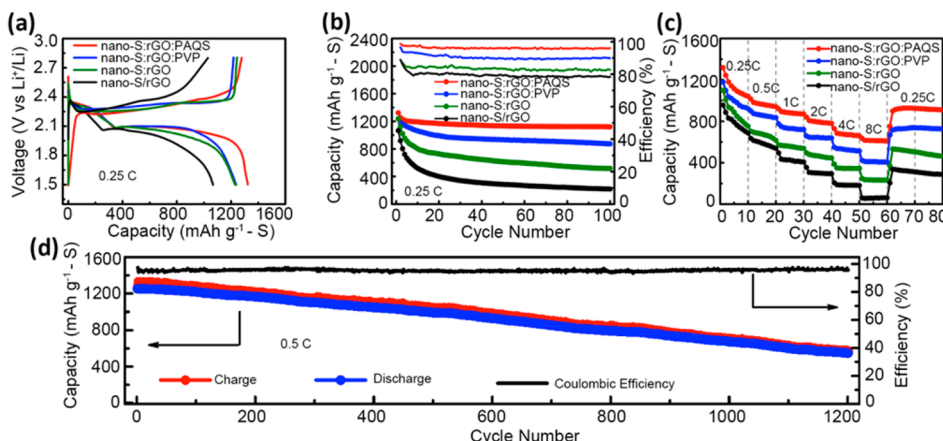


**Figure 3.** Electrochemical performance of the nano-S:rGO:PAQS composite thin film cathode. (a) Initial galvanostatic discharge/charge curves of nano-S:rGO (black), nano-S:rGO (green), nano-S:rGO:PVP (blue), and nano-S:rGO:PAQS (red) cathodes at a current density of  $418 \text{ mA g}^{-1}$  ( $1 \text{ C} = 1672 \text{ mA g}^{-1}$ ). (b) Cycling stability of nano-S:rGO (black), nano-S:rGO (green), nano-S:rGO:PVP (blue), and nano-S:rGO:PAQS (red) cathodes at a current density of  $418 \text{ mA g}^{-1}$ . (c) Rate performances of nano-S:rGO (black), nano-S:rGO (green), nano-S:rGO:PVP (blue), and nano-S:rGO:PAQS (red) cathodes. (d) Discharge capacity and Coulombic efficiency of the nano-S:rGO:PAQS cathode at a current density of  $836 \text{ mA g}^{-1}$ .

The desired structure is prepared in three steps. First, S nanoparticles are deposited onto rGO suspensions (S@rGO) via sulfur-amine chemistry as described previously.<sup>31</sup> Second, PAQS is synthesized via reductive coupling.<sup>25</sup> Finally, the PAQS polymer solution is mixed with the S@rGO suspension to allow the polymer to thoroughly adsorb on the S@rGO before the mixture is assembled into a stacked layered structure via vacuum filtration. A freestanding composite cathode (nano-S:rGO:PAQS) is then obtained after rinsing and drying.

Transmission electron micrographs (TEM) in Figure 2a–b reveal that sulfur nanoparticles approximately 10 nm in diameter are homogeneously loaded on rGO surfaces without aggregation. The X-ray diffraction (XRD) pattern (Figure 2c) shows the characteristic diffraction peaks of orthorhombic sulfur.<sup>5</sup> Figure 2d displays the Fourier transform infrared (FT-IR) spectrum of the synthesized PAQS, which is consistent with the expected structure. The C=O and C=C stretching vibrations of the anthraquinonyl group are present at 1676 and  $1568 \text{ cm}^{-1}$ , respectively, and the peak at  $1413 \text{ cm}^{-1}$  represents the stretching of the sulfur-substituted aromatic ring, all of which are consistent with previous publications (Figure 2d).<sup>24,32</sup> Scanning electron microscopy (SEM) images and energy-dispersive X-ray spectroscopy (EDX) mapping of carbon and sulfur show that the sulfur element is uniformly distributed on the rGO surface (Figure 2e–g). SEM images of the cross-section (Figure 2h,j) reveal that the self-supported film consists of unevenly stacked layers containing plenty of pores with sizes ranging from tens to hundreds of nanometers. A photograph of a freestanding nano-S:rGO:PAQS composite film is shown in Figure 2j.

It is worth noting that the composite electrode has high effective sulfur loading, 48% sulfur content in the entire cathode structure. It has been shown that in order for Li–S batteries to have the same volumetric energy density as typical LIB, the sulfur loading has to be at least 70% in the active material.<sup>9</sup> When the active material is mixed with conductive agent and binder and then pasted on current collector, the sulfur content in the entire cathode structure typically drops to about 30%. For example, when a C/S composite with 80% S loading mixed with a conductive agent and binder at a 7:2:1 ratio and pasted on Al foil (14.9  $\mu\text{m}$  thick,  $4.02 \text{ mg cm}^{-2}$ ), the sulfur content in

the entire cathode would be only 35.8%, if the areal density were to reach  $4 \text{ mg cm}^{-2}$  sulfur. Thermogravimetric (TG) analyses of the nano-S:rGO:PAQS film (Figure 2k) show steep weight loss of sulfur below  $\sim 250^\circ\text{C}$  and the decomposition of PAQS at higher temperatures. The sulfur and PAQS contents are estimated to be  $\sim 48\%$  and  $\sim 10\%$ , respectively. Because no conductive carbon, no binder, nor metal current collector is needed for the free-standing thin film cathode, the 48% sulfur content is the content in the entire cathode and is far higher than that in typical C/S composite active material based cathodes. In the example above with 80% sulfur loading active material, an extremely high areal density of  $13.4 \text{ mg cm}^{-2}$  sulfur would be required to obtain the 48% sulfur content in the entire cathode. Therefore, the electrochemical performance of this composite electrode is highly relevant and valuable.

The nano-S:rGO:PAQS cathode obtained as described above exhibits outstanding electrochemical performances, including specific capacity, rate performance and cycle stability. Comparisons with various control samples show that the improved performances originate from the synergistic effects due to the addition of PAQS, the stacked and layered rGO structure and the nanosized active sulfur materials. As shown in Figure 3, the control samples include nano-S:rGO:PVP, which is also a freestanding cathode structure where polyvinylpyrimidine (PVP) is used in place of PAQS. PVP is a commonly used binder in lithium ion and Li–S batteries with a considerable affinity toward polysulfides.<sup>33</sup> Another control sample is nano-S:rGO, which is obtained via vacuum filtration of the S@rGO suspension without the addition of either PAQS or PVP additive. The last control sample is nano-S:rGO, which is prepared by hand milling of the S@rGO sample, and the corresponding cathode is prepared by mixing the sample with a binder and conductive agent and then pasting it on an Al foil current collector. The sulfur contents in the control samples are chosen to be the same as that of the nano-S:rGO:PAQS cathode, and coin-type cells are assembled for electrochemical testing. Figure 3a shows that the nano-S:rGO:PAQS cathode displays the best initial discharging capacity of  $1323 \text{ mAh g}^{-1}$  and the highest initial Coulombic efficiency of 98.8%, indicating highly efficient sulfur utilization in the initial cycle due to the holistic rational design of the cathode structure. The nano-

S:rGO:PAQS cathode also displays the most stable cycling stability. Figure 3b shows that all cathodes have an initial fast capacity decay period that lasts for 3–5 cycles; then, the nano-S:rGO:PAQS and nano-S:rGO:PVP samples display slow decays in capacity, whereas the capacities of the nano-S:rGO and nano-S/rGO samples continue to decay quickly. The nano-S:rGO:PAQS cathode shows particularly stable cycling even compared with nano-S:rGO:PVP, indicating the importance of PAQS in capacity retention. At the end of the 100th cycle, the decay rates for nano-S:rGO, nano-S:rGO, nano-S:rGO:PVP, and nano-S:rGO:PAQS are 0.73%, 0.50%, 0.31%, and 0.15%, respectively. Notably, nano-S:rGO:PAQS possesses the highest Coulombic efficiency of more than 97% (without the addition of LiNO<sub>3</sub>), again demonstrating its significant effect in suppressing polysulfide shuttling due to the rationally designed cathode structure. Importantly, the nano-S:rGO:PAQS batteries exhibit significant rate performances (Figure 3c). They maintain a reversible capacity of ~615 mAh g<sup>-1</sup> at a rate of 13.744 A g<sup>-1</sup> (=8 C) after more than 60 cycles at various rates and can still have a reversible capacity of ~1000 mAh g<sup>-1</sup> when further cycled at 0.25 C.

With the excellent overall electrochemical performance, the nano-S:rGO:PAQS cathode was further tested for long-term cycling. As shown in Figure 3d, it exhibited a specific capacity of 1255 mAh g<sup>-1</sup> at the first discharge and 559 mAh g<sup>-1</sup> after 1200 cycles at a rate of 0.5 C while maintaining a stabilized Coulombic efficiency above 97%. The capacity decay rate is as low as 0.046% per cycles over 1200 cycles.

The excellent electrochemical performance of the nano-S:rGO:PAQS cathode can be attributed to multiple factors. First, the nanometer-sized sulfur particles are instrumental in achieving a high initial capacity, which has been discussed in depth in previous reports.<sup>5,34</sup> Here, we focus on the vital role of the PAQS polymer additive and the layered porous rGO structure in realizing stable cycling and high rate performance via the restriction of polysulfide shuttling and the facilitation of electron/ion transport.

The following *in situ* electrochemical test clearly demonstrates the restriction of polysulfide diffusion in the rationally designed nano-S:rGO:PAQS cathode. As shown in the photograph in Figure 4a–d, the designed cathode is cycled in

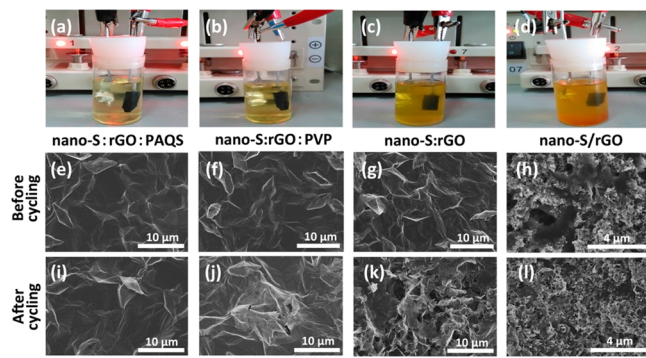


**Figure 4.** Synergistic effects limiting polysulfide dissolution and shuttling in the nano-S:rGO:PAQS cathode. (a–d) Photographs of (a) nano-S:rGO:PAQS, (b) nano-S:rGO:PVP, (c) nano-S:rGO, and (d) nano-S/rGO cathodes after 50 cycles in sealed glass cells. (e–l) *In situ* SEM images of various cathodes before and after 50 cycles in coin cells: nano-S:rGO:PAQS before (e) and after 50 cycles (i); nano-S:rGO:PVP before (f) and after 50 cycles (j); nano-S:rGO before (g) and after 50 cycles (k); nano-S/rGO before (h) and after 50 cycles (l).

a sealed glass cell against a Li anode in the same DOL/DME electrolyte as used in the coin cells. The photographs show the appearance of the glass cell after 50 cycles. Polysulfide intermediates gradually dissolve and diffuse into the electrolyte, which results in a pale yellow color. The nano-S:rGO:PVP cathode has a stronger color, indicating that more polysulfide has dissolved into the electrolyte. The nano-S:rGO cathode shows even more dissolution of polysulfide, and the electrolyte turns turbid. The nano-S/rGO cathode with neither a layered rGO structure nor a PVP or PAQS additive shows the most severe polysulfide dissolution after 50 cycles. The turbid electrolyte is a deep gold color, and a large amount of precipitate is observed in the glass cell, indicating serious irreversible loss of active sulfur. This indicates that the pore structure in these cathodes may help electrolyte permeation and Li<sup>+</sup> diffusion but are not effective in polysulfide restriction. These results are consistent with the coin cell cycling performance and indicate that polysulfide trapping additive (PAQS or PVP) and the layered rGO structure are the major effective mechanisms for the restriction of polysulfide diffusion.

Postcycling SEM characterization of electrode morphology confirms the synergistic effect of polysulfide restriction in the designed composite structures. After 50 cycles, the nano-S:rGO:PAQS cathodes display uniform, compact, and clean surfaces (Figure 4i) that appear very similar to the original morphology before cycling (Figure 4e), indicating effective suppression of polysulfide shuttling. The morphology of the nano-S:rGO:PVP cathode is also well preserved after 50 cycles, but small cracks can be observed (Figure 4f and j). In contrast, the nano-S:rGO cathode, which has a layered rGO structure but without the polysulfide trapping polymer additive, shows undesirable structural deformation after 50 cycles (Figure 4k and g). The nano-S/rGO cathode, with neither trapping additives nor layered rGO structure, is severely covered with solid deposits after 50 cycles (Figure 4l vs h), which is a typical morphology originating from insoluble discharge products due to uncontrolled polysulfide diffusion out of the cathode as previously reported.

Although the spatial confinement effect due to the porous layered rGO structure has been previously reported,<sup>14,23</sup> the effects of polysulfide-trapping polymer additives have been investigated less frequently;<sup>33</sup> in particular, the effect of PAQS has not been previously reported. Previous reports on polysulfide trapping reagents have shown that organic molecules with carbonyl groups are expected to interact with lithium polysulfides and, thus, may stabilize Li–S battery cycling.<sup>33</sup> Both PVP and PAQS are rich in carbonyl groups, but PAQS apparently exhibits a stronger polysulfide trapping effect. Here, density functional theory (DFT) calculations are performed to further understand the PAQS trapping effect. The detailed setup of the calculation (Supporting Information) follows a previous publication, where the Li–S<sup>–</sup> species was used to represent the relevant end groups in the general class of lithium polysulfides (Li–S–S<sub>n–2</sub>–S–Li; Li<sub>2</sub>S<sub>n</sub> in short, 4 ≤ n ≤ 8).<sup>33</sup> As shown in Table 1, the binding energies between PVP

**Table 1. Binding Energies of Li<sub>2</sub>S and Li–S<sup>–</sup> Species with PAQS and PVP Obtained from DFT Calculations**

	binding energy with Li <sub>2</sub> S (eV)	binding energy with Li–S <sup>–</sup> (eV)
PAQS	2.1	2.53
PVP	1.18	0.93

and Li<sub>2</sub>S and Li-S<sup>-</sup> are 1.18 and 0.93 eV, respectively, which is in good agreement with the results reported by Cui et al.<sup>32</sup> The binding energies between PAQS and Li<sub>2</sub>S and Li-S<sup>-</sup> are 2.1 and 2.5 eV, respectively, which are significantly stronger than that of PVP, thus explaining its superior electrochemical properties in the coin cell tests. The energy minimized configuration of the interacting pairs (Figure 5) shows that

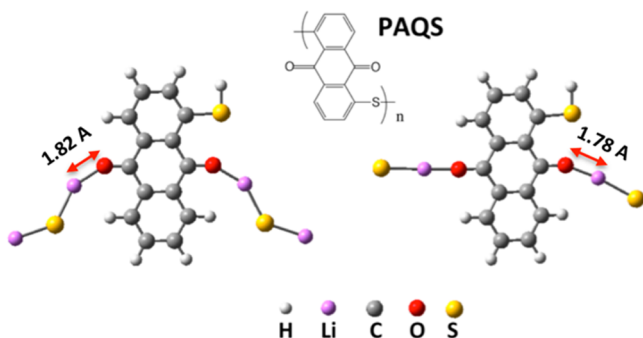


**Figure 5.** Most stable configurations of PAQS interacting with Li<sub>2</sub>S and Li-S<sup>-</sup> obtained using DFT calculations.

the electron-rich carbonyl group interacts with a lithium ion in both Li<sub>2</sub>S and Li-S<sup>-</sup> via the lone pairs on the oxygen atom, forming a coordination-like Li-O bond.<sup>33</sup> This interaction pattern is consistent with previous publications on the interaction between polysulfides and organic molecules.<sup>35,36</sup> The conjugated units in the PAQS backbone and the consequently more rigid molecular conformation may contribute to its particularly strong interaction with lithium sulfides. In addition, the “π-π” interaction between conjugated aromatic PAQS with graphene may assist uniform dispersion of PAQS within the layered rGO matrix and improve the mechanical adhesion between these two components,<sup>25</sup> which would further enhance the stability of the composite cathode structure and, consequently, result in better cycling.

The outstanding property of PAQS in the composite Li-S cathode may also be related to another function of PAQS as an excellent Li<sup>+</sup> conductor. PAQS is a redox active molecule (Supporting Information Scheme S1) and, thus, has been suggested to be used as the active material for a high power organic battery.<sup>24,25</sup> In a cathode structure with PAQS in situ polymerized on graphene sheets, a capacity of 100 mAh g<sup>-1</sup> can be reached even at a 100 C discharging rate (1 C = 225 mA g<sup>-1</sup>, 22.5 A g<sup>-1</sup>).<sup>25</sup> The impressive rate performance is attributed to not only the fast redox kinetics of quinone groups but also the

unique Li<sup>+</sup> conduction property of PAQS.<sup>25</sup> We repeated the test using a PAQS:rGO structure, where a PAQS solution is mixed with an rGO dispersion without sulfur, and the mixture is vacuum filtered to obtain a freestanding electrode (Supporting Information). As shown in Supporting Information Figure S1, the electrode shows discharge capacities at high rates similar to those of in situ polymerized PAQS/rGO, confirming the fast kinetics and potentially fast Li<sup>+</sup> conduction of PAQS cathodes.

The charge transfer resistance and effective diffusion coefficients of Li<sup>+</sup> ions in the two polymer-containing cathodes nano-S:rGO:PAQS and nano-S:rGO:PVP are evaluated from the corresponding electrochemical impedance (EIS) spectra. The EIS spectra of freshly prepared coin cells (Figure 6a) show a depressed semicircle in the high frequency region followed by an inclined line in the low frequency region. The spectra are analyzed and fit with an equivalent circuit model published in previous literature, in which  $R_e$  represents the impedance of the electrolyte.  $R_{ct}$  is the charge transfer resistance, and a constant phase element (CPE) is used to represent the capacitance of the electrical double layer.<sup>37,38</sup> The fitting yields a charge transfer resistance of 30 ohms for the nano-S:rGO:PAQS cathode and 46 ohms for the nano-S:rGO:PVP cathode, which indicates that PAQS may help to reduce the charge transfer resistance and, thus, contribute to the superior rate performance.

Because there are no complex polysulfide species in the electrode in freshly prepared cells, the inclined line in the low frequency region is attributed to the diffusion of Li<sup>+</sup> in the composite cathode structure.<sup>39</sup> The effective Li<sup>+</sup> diffusion coefficient D in the composite cathode can be obtained from eq 1<sup>40</sup>

$$D = 0.5 \left( \frac{RT}{AF^2 \sigma_\omega C} \right)^2 \quad (1)$$

where R is the gas constant, T is the temperature, A is the area of the electrode surface, F is Faraday's constant, C is the molar concentration of Li<sup>+</sup> in the electrolyte, and  $\sigma_\omega$  is the Warburg factor, that is, the slope for the plot of  $Z'$  vs the reciprocal root square of the lower angular frequencies ( $\omega^{-1/2}$ ), obtained from eq 2

$$Z' = \sigma_\omega \omega^{-0.5} \quad (2)$$

Figure 6b shows the fitting of eq 2, and the Li<sup>+</sup> diffusion coefficients are calculated. The effective Li<sup>+</sup> diffusion coefficient in the nano-S:rGO:PAQS cathode ( $4.8 \times 10^{-8}$  cm<sup>2</sup> s<sup>-1</sup>) is

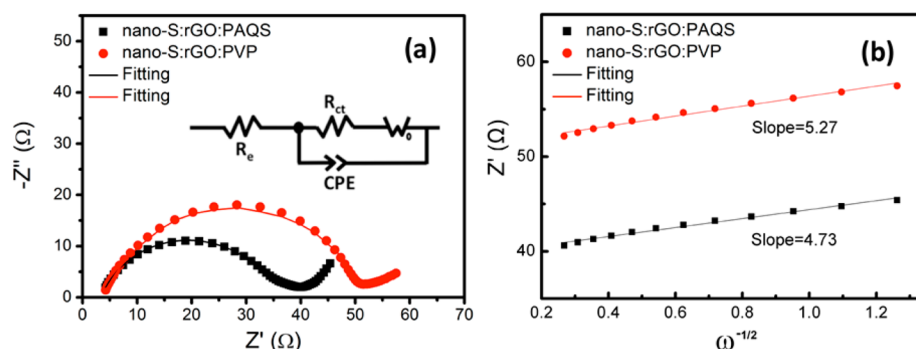


**Figure 6.** (a) EIS of assembled nano-S:rGO:PVP and nano-S:rGO:PAQS coin cells. The inset figure is the equivalent circuit used to fit the impedance spectra. (b) Plot of  $Z'$  vs  $\omega^{-1/2}$  in the low frequency region.

higher than that in the nano-S:rGO:PVP cathode ( $3.9 \times 10^{-8}$  cm<sup>2</sup> s<sup>-1</sup>), indicating that the better Li<sup>+</sup> kinetics in the nano-S:rGO:PAQS battery may result from the PAQS additive.

In conclusion, a high performance Li–S cathode is designed and demonstrated in this work. The freestanding composite film nano-S:rGO:PAQS consists of nanosized sulfur particles on rGO sheets and the multifunctional polymer additive PAQS. The film is obtained via simple vacuum filtration and can be used as an electrode without a metal current collector or an additional conducting agent. The layered and porous rGO structure provides electron and ion transfer paths, accommodates volume changes in cycling, restricts polysulfide diffusion, and thus suppresses polysulfide shuttling. PAQS strongly traps polysulfides, which also suppresses polysulfide shuttling. Moreover, PAQS is an excellent Li<sup>+</sup> conductor and contributes to the improvements in the rate performance. With the synergistic effects originating from the sulfur nanoparticles, layered porous rGO structure and PAQS additive, the resulting Li–S battery exhibited a specific capacity of 1255 mAh g<sup>-1</sup> at the first discharge and 559 mAh g<sup>-1</sup> after 1200 cycles at 0.5 C, keeping the Coulombic efficiency stabilized above 97%. The capacity decay rate is as low as 0.046% per cycle over 1200 cycles. Importantly, the battery exhibited a significant rate performance of 615 mAh g<sup>-1</sup> at a high rate of 8 C. We believe the holistic design approach targeting not only specific capacity and cycle life but also rate performance is an essential step toward the practical application of Li–S technology.

## ■ ASSOCIATED CONTENT

### Supporting Information

Experimental procedures and additional electrochemical characterization. The Supporting Information is available free of charge on the ACS Publications website at DOI: 10.1021/acs.nanolett.5b01837.

## ■ AUTHOR INFORMATION

### Corresponding Author

\*E-mail: lwchen2008@sinano.ac.cn

### Author Contributions

<sup>†</sup>These authors contributed equally to this work.

### Notes

The authors declare no competing financial interest.

## ■ ACKNOWLEDGMENTS

This work was supported by the “Strategic Priority Research Program” of the CAS (grant No. XDA09010600), the National Natural Science Foundation of China (grant Nos. 21473242, 21273273), and Sci. & Tech. Projects of Suzhou (ZXJ2012002). L.C. acknowledges the support from Jiangsu Provincial Natural Science Foundation (Grant No. BK20130006).

## ■ REFERENCES

- (1) Xin, S.; Guo, Y. G.; Wan, L. *J. Zhongguo Kexue: Huaxue* **2011**, *41*, 1229–1239.
- (2) Bruce, P. G.; Freunberger, S. A.; Hardwick, L. J.; Tarascon, J.-M. *Nat. Mater.* **2012**, *11*, 19–29.
- (3) Zhang, S. S. *J. Power Sources* **2013**, *231*, 153–162.
- (4) Yin, Y. X.; Xin, S.; Guo, Y. G.; Wan, L. *J. Angew. Chem., Int. Ed.* **2013**, *52*, 13186–13200.
- (5) Chen, H.; Wang, C.; Dong, W.; Lu, W.; Chen, L. *Nano Lett.* **2015**, *15*, 798–802.
- (6) Wei Seh, Z.; Li, W.; Cha, J. J.; Zheng, G.; Yang, Y.; McDowell, M. T.; Hsu, P.-C.; Cui, Y. *Nat. Commun.* **2013**, *4*, 1331.
- (7) Mikhaylik, Y. V.; Kovalev, I.; Schock, R.; Kumaresan, K.; Xu, J.; Affinito, J. *ECS Trans.* **2010**, *25*, 23–34.
- (8) Xu, W.; Wang, J.; Ding, F.; Chen, X.; Nasibulin, E.; Zhang, Y.; Zhang, J. *Energy Environ. Sci.* **2014**, *7*, 513–537.
- (9) Yang, Y.; Zheng, G.; Cui, Y. *Chem. Soc. Rev.* **2013**, *42*, 3018–3032.
- (10) Park, M.; Zhang, X.; Chung, M.; Less, G. B.; Sastry, A. M. *J. Power Sources* **2010**, *195*, 7904–7929.
- (11) Yamin, H.; Goreshtein, A.; Penciner, J.; Sternberg, Y.; Peled, E. *J. Electrochem. Soc.* **1988**, *135*, 1045–1048.
- (12) Xu, R.; Belharouak, I.; Li, J.; Zhang, X.; Bloom, I.; Bareño, J. *Adv. Energy Mater.* **2013**, *3*, 833–838.
- (13) Ji, L.; Rao, M.; Zheng, H.; Zhang, L.; Li, Y.; Duan, W.; Guo, J.; Cairns, E. J.; Zhang, Y. *J. Am. Chem. Soc.* **2011**, *133*, 18522–18525.
- (14) Wang, H.; Yang, Y.; Liang, Y.; Robinson, J. T.; Li, Y.; Jackson, A.; Cui, Y.; Dai, H. *Nano Lett.* **2011**, *11*, 2644–2647.
- (15) Jayaprakash, N.; Shen, J.; Moganty, S. S.; Corona, A.; Archer, L. A. *Angew. Chem.* **2011**, *123*, 6026–6030.
- (16) Zhang, C.; Wu, H. B.; Yuan, C.; Guo, Z.; Lou, X. W. D. *Angew. Chem.* **2012**, *124*, 9730–9733.
- (17) Zhang, K.; Zhao, Q.; Tao, Z.; Chen, J. *Nano Res.* **2013**, *6*, 38–46.
- (18) Evers, S.; Nazar, L. F. *Acc. Chem. Res.* **2012**, *46*, 1135–1143.
- (19) Ma, J.; Fang, Z.; Yan, Y.; Yang, Z.; Gu, L.; Hu, Y. S.; Li, H.; Wang, Z.; Huang, X. *Adv. Energy Mater.* **2015**, n/a.
- (20) Elazari, R.; Salitra, G.; Garsuch, A.; Panchenko, A.; Aurbach, D. *Adv. Mater.* **2011**, *23*, 5641–5644.
- (21) Zhou, G.; Wang, D.-W.; Li, F.; Hou, P.-X.; Yin, L.; Liu, C.; Lu, G. Q. M.; Gentle, I. R.; Cheng, H.-M. *Energy Environ. Sci.* **2012**, *5*, 8901–8906.
- (22) Yuan, Z.; Peng, H. J.; Huang, J. Q.; Liu, X. Y.; Wang, D. W.; Cheng, X. B.; Zhang, Q. *Adv. Funct. Mater.* **2014**, *24*, 6105–6112.
- (23) Evers, S.; Nazar, L. F. *Chem. Commun.* **2012**, *48*, 1233–1235.
- (24) Song, Z.; Zhan, H.; Zhou, Y. *Chem. Commun.* **2009**, 448–450.
- (25) Song, Z.; Xu, T.; Gordin, M. L.; Jiang, Y.; Bae, I.; Xiao, Q.; Zhan, H.; Liu, J.; Wang, D. *Nano Lett.* **2012**, *12*, 2205–2211.
- (26) Chen, H.; Müller, M. B.; Gilmore, K. J.; Wallace, G. G.; Li, D. *Adv. Mater.* **2008**, *20*, 3557–3561.
- (27) Compton, O. C.; Dikin, D. A.; Putz, K. W.; Brinson, L. C.; Nguyen, S. T. *Adv. Mater.* **2010**, *22*, 892–896.
- (28) Wang, C.; Li, D.; Too, C. O.; Wallace, G. G. *Chem. Mater.* **2009**, *21*, 2604–2606.
- (29) Yoo, E.; Kim, J.; Hosono, E.; Zhou, H.-s.; Kudo, T.; Honma, I. *Nano Lett.* **2008**, *8*, 2277–2282.
- (30) Yang, C.; Yin, Y.; Guo, Y.; Wan, L. *J. Am. Chem. Soc.* **2015**, *137*, 2215–2218.
- (31) Wang, C.; Chen, H.; Dong, W.; Ge, J.; Lu, W.; Wu, X.; Guo, L.; Chen, L. *Chem. Commun.* **2014**, *50*, 1202–1204.
- (32) Lee, W.; Suzuki, S.; Miyayama, M. *Nanomaterials* **2014**, *4*, 599–611.
- (33) WeiáSeh, Z.; Zhang, Q.; Li, W.; Zheng, G.; Yao, H.; Cui, Y. *Chem. Sci.* **2013**, *4*, 3673–3677.
- (34) Chen, H.; Dong, W.; Ge, J.; Wang, C.; Wu, X.; Lu, W.; Chen, L. *Sci. Rep.* **2013**, *3*, 1910.
- (35) Wang, Z.; Dong, Y.; Li, H.; Zhao, Z.; Wu, H. B.; Hao, C.; Liu, S.; Qiu, J.; Lou, X. W. D. *Nat. Commun.* **2014**, *5*, 5002.
- (36) Song, J.; Gordin, M. L.; Xu, T.; Chen, S.; Yu, Z.; Sohn, H.; Lu, J.; Ren, Y.; Duan, Y.; Wang, D. *Angew. Chem.* **2015**, *127*, 4399–4403.
- (37) Cañas, N. A.; Hirose, K.; Pascucci, B. *Electrochim. Acta* **2013**, *97*, 42–51.
- (38) Deng, Z.; Zhang, Z.; Lai, Y.; Liu, J.; Li, J.; Liu, Y. *J. Electrochem. Soc.* **2013**, *160*, A553–A558.
- (39) Yuan, L.; Qiu, X.; Chen, L.; Zhu, W. *J. Power Sources* **2009**, *189*, 127–132.
- (40) Cui, Y.; Zhao, X.; Guo, R. *Electrochim. Acta* **2010**, *55*, 922–926.